Numerical investigation of multiple wingsails interaction under different apparent wind angles

Ocean Engineering 336 (2025) 121712

Contents lists available at ScienceDirect

Ocean Engineering

journal homepage: www.elsevier.com/locate/oceaneng

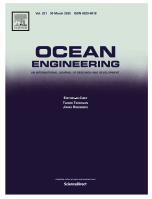

Research paper

Numerical investigation of multiple wingsails interaction under different apparent wind angles

Kewei Xu [a,b,1,*], Karolina Malmek [c,2], Rickard Bensow [b,3]

[a] Department of Mechanical Engineering, University of Maine, Orono, 04469, USA
[b] Department of Mechanics and Maritime Sciences, Chalmers University of Technology, Gothenburg, 41296, Sweden
[c] Maritime Department, RISE Research Institutes of Sweden, Gothenburg, 41258, Sweden

ARTICLE INFO

Keywords:
Wind propulsion
Wingsail interactions
Aerodynamics
CFD
Fluctuation

ABSTRACT

In the context of enhancing sustainability, wind propulsion using wingsails has emerged as a promising solution to reduce emissions in the maritime sector. This paper numerically studies a model-scale three-wingsail system to understand the interaction mechanism of multiple wingsails. Improved Delayed Detached Eddy Simulation (IDDES) is conducted with $k-\omega$ SST model and is validated by wind tunnel testing data. Two apparent wind angles (AWAs) of 30° and 90°, standing for representative wingsail-interaction scenarios are chosen and each AWA is studied with a low and high angle of attack (AoA). At AWA of 30°, the individual wingsail is subjected to the downwash or upwash effects generated by adjacent wingsails, leading to the variation of stagnation point location and performance change. At AWA of 90° where wingsails are located in the same streamwise position, adjacent wingsails interact through the pressure-field interaction, which impairs each other's performance. At high AoA, the flow separation occurs at the low span of the wingsail due to the sluggish flow in the floor boundary layer. As compared to the single sail case, the interaction effect makes the flow separation more severe in the leading wingsail. In this regard, the vortical behavior is also amplified as indicated by proper orthogonal decomposition (POD) analysis, leading to an enhanced force fluctuation.

1. Introduction

Maritime transport is responsible for more than 80 % of the volume of international trade in goods, however, it is also a major source of greenhouse gas (GHG) emissions. According to recent estimates, maritime transport emits around 940 million tonnes of CO2 annually, accounting for about 3 % of global greenhouse gas emissions. This figure is predicted to increase by up to 50 % by 2050 if the industry continues on its current trend (Smith et al., 2015). Such projections underscore the urgent need for sustainable practices. Recognizing this, governments and international bodies have started implementing concrete measures for emission reduction. The International Maritime Organization (IMO), for instance, has recently revised its GHG Strategy, setting a target to reduce the carbon intensity of international shipping by at least 40 % by 2030. The strategy also includes an enhanced ambition to reach net-zero GHG emissions close to 2050 (IMO, 2023). Under this background, Wind Propulsion Technologies (WPTs), such as wingsails, Flettner rotors, kites, etc., emerge as viable solutions to address the sustainability issues (Khan et al., 2021). Unlike the traditional soft sails, wingsail is a rigid, airfoil-shaped sail with significantly higher propulsive efficiency, which can reduce engine fuel consumption by 10 % up to an estimated 90 %, depending on vessel type and operational conditions. In this regard, modern wingsail technologies are widely studied. Fig. 1 is the concept of car carriers proposed by Oceanbird.

Ouchi et al. (2011) numerically studied the flow field of a wind-powered vessel with nine sails under various apparent wind angles (AWA). The power-saving performance was demonstrated through a case study in the Pacific trade wind region. Viola et al. (2015) developed an optimization method for AC72 (American's cup) rigid wingsail based on a mesh morphing technique which is integrated into a Reynolds-averaged Navier-Stokes equations (RANS) solver. The method's effectiveness was demonstrated through the optimization of trim angles of the two wing elements and angles of attack. Li et al. (2015) conducted both numerical and experimental studies on their proposed variable camber sail (VCS) and a maximum lift coefficient (C_L) of about 1.5 was achieved. Lee et al. (2016) developed a design optimization

* Corresponding author.
E-mail address: kewei.xu@maine.edu (K. Xu).
[1] Assistant Professor, University of Maine.
[2] PhD Candidate, The Safety and Transport Division.
[3] Full Professor, Division of Marine Technology.

https://doi.org/10.1016/j.oceaneng.2025.121712
Received 24 November 2024; Received in revised form 20 May 2025; Accepted 28 May 2025
Available online 11 June 2025

Fig. 1. Concept design of the Oceanbird wingsail ship (Oceanbird, 2021).

framework using the genetic algorithm and the Kriging surrogate model to maximize the thrust coefficient for multiple wingsails. The optimized angle of attack (AoA), flap deflection length, and flap deflection angle were obtained. Verified through three-dimensional RANS simulation, the thrust performance was improved by 10 % ~ 17 %. Atkinson (2019) numerically studied the aerodynamic performance of a segmented rigid wingsail using three-dimensional CFD simulation. The wingsail was found to be able to produce an equal amount of maximum C_L and maximum drag coefficient (C_D), which all contributed to thrust generation. Cairns et al. (2021) numerically studied Co-flow Jet (CFJ) (Xu and Zha., 2021; Xu et al.(2022)Xu, Ren and Zha; Xu et al., 2021) active flow control on a two-dimensional wingsail airfoil. Through the application of a Kriging model and genetic algorithm, the optimized CFJ wingsail possessed a robust performance curve over the expected operating range and the maximum C_L was improved by 13.17 %. Zhu et al. (2023, 2024) studied a crescent-shaped wingsail using unsteady-RANS and Improved Delayed Detached Eddy Simulation (IDDES). They found that the crescent-shaped wingsail had a higher propulsion efficiency than the NACA symmetric ones due to its more chambered geometry. However, this benefit came with the price of stronger flow separations, which increased flow unsteadiness.

To maximize the utilization of wind energy the total sail area should be as large as possible. For practical reasons, such as limitations in the manufacturing process and the on-board installation, this sail area is normally divided into multiple sails. Therefore, the interaction effects among wingsails attract particular interest. The experimental investigations by Fujiwara et al. (2005) highlighted the interactive loss of driving force and yaw moment. A type of hybrid sail with rigid and soft parts was studied in rectangular and triangular shapes, respectively. It was found that the interaction loss can be recovered by more than 5 % by adopting a graduated arrangement or a goose-winged arrangement rather than a parallel arrangement of the sails. The numerical studies (Ouchi et al., 2011) on a nine-sail wind propulsion system indicated that the thrust loss due to interaction was more severe under low AWA of 30° and was alleviated as AWA increased. Li et al. (2015) found that the overall performance of the multi-wingsail system was strongly subjected to the distance between wingsails. Moreover, it was reported by Lee et al. (2016) that the interaction effect reduced the thrust coefficient of VCS multiple wingsails by 21–43 % depending on AWA, as compared to that of the single sail cases. Bordogna (January 2020) numerically investigated a two-sail arrangement Dynarig wind-assisted device and found that the interaction had a positive effect on both sails under moderate AWAs, whereas possessed a negative effect for the downstream sail in either smaller or larger AWAs. Giovannetti et al. conducted wind tunnel experiments for three interacting wingsails based on an early version of the Oceanbird wingsail concept (Giovannetti et al., 2022). Using the same test case, Malmek et al. (2024) studied the sail-sail interaction and developed a rapid method for wingsail performance predictions based on a semi-empirical lifting line model with a potential flow-based interaction model. The results produced by the rapid method were validated against RANS simulation and the experimental testing (Malmek, 2023).

Overall, the previous studies on wingsail interactions mainly focus on the performance sensitivity to different free-stream conditions including AoA, AWA, wind speed, Reynolds number (Re), etc., or to various geometrical configurations such as sail shapes and sail distance. Limited efforts are made to understand the mechanism that is responsible for the performance variations. Questions of interest include what is the interaction mechanism between downstream and upstream wingsails and how is the interaction between wingsails in the same streamwise location (e.g. at AWA of 90°). There are some early studies on the interaction effects between jib and mainsail (Gentry, 1971, 1981), but the efforts were in two dimensional and sails were located significantly closer than they were nowadays. Moreover, the previous research mainly studies the time-averaged interactive performance. As the AoA increases, the flow starts to separate from the wingsails and raises the flow unsteadiness. Which sail is prone to flow separation and how is the fluctuating quantity affected by interaction effects are the key questions to be addressed. An advanced understanding of these questions is essential for the development of proper sail configurations, the design of high-efficient flow control methods, and the operation of sails. This study is to shed some light on these subjects. Moreover, in the aerospace community, there are certain studies to understand the physics of wing-wing interactions. However, the interests are mostly confined to two wings (Tu, 1994; Myose et al., 1997; Shah and Ahmed, 2024; Kleinert et al., 2024) or the interaction in flapping wing aircraft with very low Re (Tay, 2017; Lehmann et al., 2005). The mechanism reasoning regarding multiple wings' interaction in the current manner is rare.

This paper numerically investigates the interaction mechanism in a model-scale three-wingsail system where each sail is stacked using a NACA0015 airfoil. There are two AWAs of interest, 30° and 90°, representing different sail-sail interaction scenarios due to the different streamwise locations of sails. Each AWA is investigated at a low and a high AoA to understand the wingsail interactions with the attached flow and with flow unsteadiness, respectively. To better highlight the interaction effect, single sail cases are also simulated as a reference. The numerical simulations are conducted using IDDES with $k-\omega$ SST model and are validated by wind tunnel testing data. At low AoA, the interaction mechanism is studied by analyzing the movement of stagnation points, variations of effective AoA, and velocity contours. At high AoA, power spectrum density (PSD) analysis is conducted on the force histories of wingsails to filter dominant fluctuations. Furthermore, their corresponding unsteady behaviors are interpreted through proper orthogonal decomposition (POD) of flow fields, and the interaction effects on fluctuating quantities are better understood.

The remainder of the paper is organized as follows: Section 2 introduces the model and experimental setups, including model specifications, wind tunnel facilities, and test conditions. Section 3 describes the numerical setup and validations, including numerical methods, boundary conditions, grid dependency studies, and validation against experimental data. Section 4 presents the results for multiple wingsail and single sail cases at the two AoAs and two AWAs. The discussion of the interaction mechanism is provided based on the acquired results.

2. Model geometry and experimental results

The multiple wingsail geometry and experimental results come from the experimental study conducted by Giovannetti et al. (2022) as a part of the WPCC/Oceanbird project. The experiments were carried out at the R.J. Mitchell wind tunnel at the University of Southampton, with a tunnel test section of 3.5 m × 2.4 m and a turbulence intensity level of less than 0.2 %.

The geometry of the model consisted of three wingsails using a NACA0015 airfoil profile with a slightly modified tapering toward the tip. This wingsail geometry has been used as a test case in several stud-

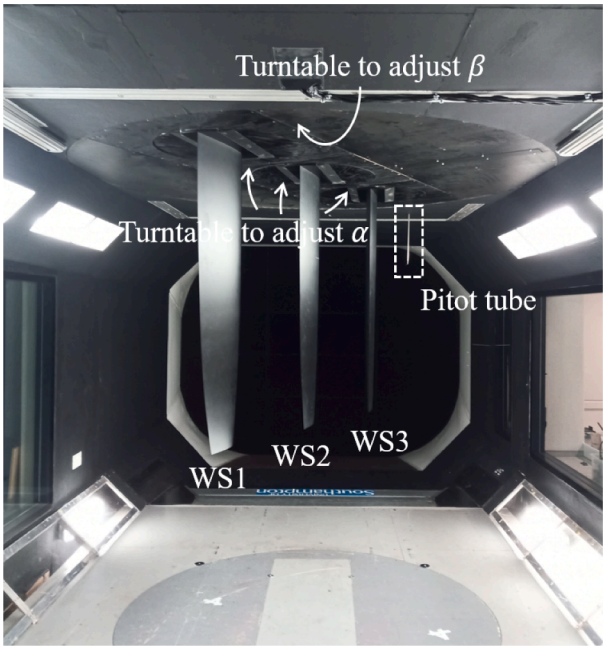

Fig. 2. Picture of the wind tunnel and the wingsail model. Courtesy of the WPCC/Oceanbird project (Giovannetti et al., 2022).

Table 1
Geometrical parameters of wingsails.

2D profile	NACA 0015
Span	1.385m
Averaged chord	0.4 m
Single sail area	0.552 m^2
Wingsail spacing	0.748 m
Number of sails	3

ies (Persson et al., 2019; Malmek, 2023) and was scaled 1:58 in the experiments. Fig. 2 shows the model setup in the tunnel. The average chord length (C) was 400 mm and the span (b) was 1385 mm. The mast-to-mast spacing (MMS) was 748 mm. Further model dimensions are presented in Table 1. The angle of attack (AoA, α) was adjusted by rotating each wingsail about its 25 % chord (C). The apparent wind angle (AWA, β), defined as the angle between the sailing vessel's heading and the apparent wind, was adjusted by rotating the tunnel roof turntable.

The experiments were conducted at a free-stream velocity U_∞ of 25 m/s, which corresponded to a Reynolds number (Re) of 7.62×10^5. To stimulate a turbulent flow regime over the three wingsails, an aerodynamic boundary layer (BL) trip tape was applied on the suction and pressure sides of the wings at 25 %C (Malmek, 2023). This BL trip tape is not included in the numerical simulations presented in this study. During the experiments, the total aerodynamic forces of the three wingsails were measured via a six-component Nuntem load cell balance. Each sail's forces were measured by three force and moment transducers. The experimental uncertainty in lift and drag force prediction has been evaluated in the single-sail experiments (Wielgosz et al., 2025). Pressure distributions were collected on the mid-sail. Three spanwise locations were chosen to collect C_p data: 33 %, 60 %, and 80 % measured from root to tip. The middle sail was selected for validation because it experiences close flow interaction from both the sail in front and the aft-most sail. This choice ensured that both upstream and downstream effects were captured. Constraints in experimental resources, including time and cost of installing and calibrating pressure taps, necessitated focusing on one sail position. Also, the benefit of additional flow data was deemed limited as the major focus of the experimental campaign was to collect force measurements for a large number of different angles of attack and apparent wind angles to identify, for example, the point of stall under various interaction conditions.

3. Numerical setup and validations

The Improved Delayed Detached Eddy Simulation (IDDES) is conducted using the commercial finite volume software, Star-CCM+. As a hybrid model, IDDES uses Large Eddy Simulation (LES) to resolve large turbulent motions as well as unsteady Reynolds-averaged Navier-Stokes (RANS) resolution in the boundary layer to save near-wall modeling time. The two-equation $k-\omega$ SST turbulence model is used in the RANS part. IDDES is well-performed in wingsails flow predictions (Zhu et al., 2024).

The convective flux is evaluated by a bounded central-differencing scheme that blends 98 % of the second-order central differencing scheme and 2 % of the first-order upwind scheme for robustness purposes. The diffusive fluxes use second-order central differencing. The implicit unsteady solver with the second-order Euler implicit scheme is used to approximate the transient term. The physical time step (Δt) is 2×10^{-4} s to keep the maximum CFL (Courant Friedrichs Lewy) number lower than 10. A similar CFL criterion is also adopted in another wingsail numerical study (Zhu et al., 2024). This is because the implicit solver has an enhanced numerical stability as compared to the explicit scheme and, therefore, allows larger time steps and higher CFL numbers. The simulation is run from scratch, and after a characteristic time ($t^*=tU_\infty/C$) of 63 when all the aerodynamic forces become dynamically stable, the IDDES simulation begins sampling and averaging results for t^* of 188. The present IDDES simulation is conducted using the Tetralith general computing resource provided by SNIC (Swedish National Infrastructure for Computing) at the National Academic Infrastructure for Supercomputing in Sweden (NAISS). Each case requires about 25,000 CPU hours and 768 cores (Intel Xeon Gold 6130 processors).

Fig. 3 shows the computational domain with a length of 33.3C, a width of 8.8C and a height of 6.0C. The width and height match the exact wind tunnel dimension, while the length is extended by putting the outlet 50 % further downstream to have sufficient length for disturbance dissipation. The cross-section is octangular, the same as the wind tunnel shape. The coordinates system and velocity direction are denoted by x and u in the streamwise direction, y and v in the side (lateral) direction, and z and w in the spanwise (vertical) direction. The inlet is applied with a uniform velocity inlet boundary condition. The free-stream velocity (U_∞) and Reynolds number (Re) are kept the same as those in the experiments. Turbulent intensity is applied with 0.2 %, and no particular treatment is conducted for the free-stream turbulence. A static pressure outlet is specified at the outlet. Wingsail surfaces and all wind tunnel walls are applied with the no-slip wall boundary condition.

The structured hexahedral mesh is created using Pointwise. Fig. 4 shows the details of the mesh topology. An O-type mesh is created around each wingsail and is connected with an H-type mesh in downstream and upstream. For mesh quality purposes, the sharp trailing edge is cut by 0.3 %C and is replaced by a circular shape as shown in the zoom-in view in Fig. 4. The initial mesh size contains 47 million cells. The first grid distance of wingsail surfaces Δy is 1.2×10^{-5}m, which ensures $y^+=\frac{\Delta y u_\tau}{\nu}$ lower than 1. 40 cells are placed within 10 %C near the wingsail surface for boundary layer refinement. The y^+ of the wind tunnel walls is 49 and is therefore modeled using the blended wall function. There are 500 cells placed around each wingsail circumferentially and 270 cells along the span.

The numerical validation is conducted at apparent wind $\beta=30°$ and angle of attack α at 13°, 15°, and 17° for the first, middle, and last wingsails, respectively. The predicted lift coefficient (C_L), drag coefficient (C_D), and pressure coefficient distribution (C_p) are compared with the experimental data (Giovannetti et al., 2022). Normalization of these

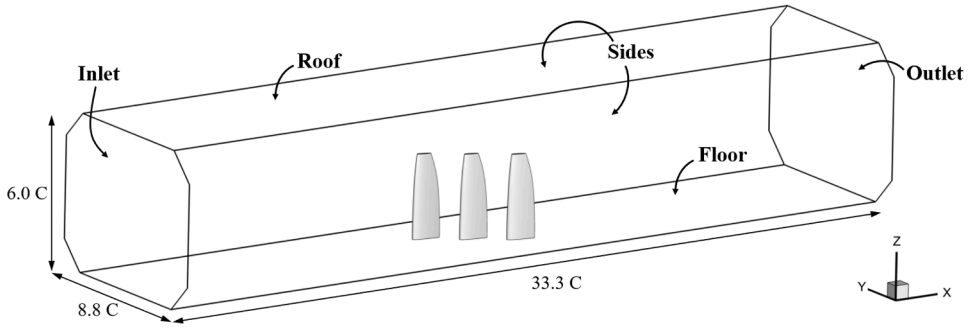

Fig. 3. Computational domain and boundary conditions.

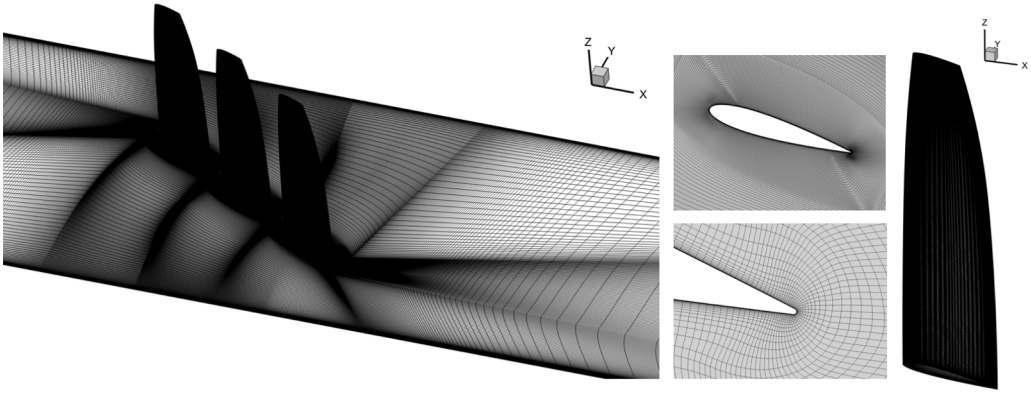

Fig. 4. Mesh topology ($\beta = 30°$).

Table 2
Comparisons between numerical and experimental results (Persson et al., 2019; Malmek, 2023) at $\beta = 30°$ and α at 13°, 15°, and 17°.

Case	WS1, 13°		WS2, 15°		WS3, 17°	
	$\overline{C_L}$	$\overline{C_D}$	$\overline{C_L}$	$\overline{C_D}$	$\overline{C_L}$	$\overline{C_D}$
Initial	1.271	0.051	1.043	0.118	0.860	0.141
Fine	1.278	0.052	1.050	0.123	0.860	0.143
EXP	1.222	0.053	1.02	0.124	0.848	0.136
Δ	4.00 %	1.89 %	2.25 %	4.84 %	1.4 %	3.6 %

coefficients follows Eqs. (1) - (3):

$$C_L = \frac{L}{0.5\rho_\infty {U_\infty}^2 S} \tag{1}$$

$$C_D = \frac{D}{0.5\rho_\infty {U_\infty}^2 S} \tag{2}$$

$$C_p = \frac{p - p_\infty}{0.5\rho_\infty {U_\infty}^2} \tag{3}$$

where L and D are the integration of pressure and shear stress in y and x direction, respectively, ρ_∞ is the free-stream density, S is the wingsail reference area, and p_∞ is the free-stream pressure.

Table 2 compares the time-averaged $\overline{C_L}$ and $\overline{C_D}$ acquired by the initial mesh and experimental testing. The value Δ quantifies the discrepancy between the numerical results from the initial mesh and experimental results. As it is suggested, the predicted $\overline{C_L}$ and $\overline{C_D}$ using the current numerical setups and mesh size achieve a good agreement with the experimental data for all three sails. The maximum discrepancy is less than 5 %.

Then, the time-averaged $\overline{C_p}$ at three span locations of the mid-sail, 33 %, 60 % and 80 % are used for further validation. Gauge pressure is used to calculate $\overline{C_p}$ throughout the paper. As shown in Fig. 5, the predicted $\overline{C_p}$ distributions at three spanwise locations achieve good agreement with the experimental data. A minor discrepancy is observed on the suction surface towards the trailing edge (TE).

A mesh dependency study is conducted using a fine mesh of 60 million cells. The fine mesh is created by increasing the resolution in the wingsail's normal-wall direction by 50 % and increasing streamwise resolution downstream of the wingsail by 25 % to better resolve the wake. Table 2 shows that the acquired $\overline{C_D}$ and $\overline{C_L}$ using fine mesh achieve a slight difference from those predicted by the initial mesh. The $\overline{C_p}$ distributions in Fig. 5 further support the convergence of the initial mesh size, as the predicted $\overline{C_p}$ distributions acquired by the two meshes are virtually overlapped. Overall, the current numerical method is capable of predicting the flow around multiple wingsails with satisfactory accuracy, and the result is converged on the initial mesh size of 47 million cells.

4. Results and discussions

This section presents the wingsail performance in two angles of attack (AoA), a relatively low AoA of 10° and a high AoA of 17°. In each AoA, two apparent wind angles (AWA) are studied, 30° and 90° as shown in Fig. 6. AWA of 30° represents sailing close hauled where the total driving force is usually low due to the lift force being almost orthogonal to the driving direction. Under such an AWA, the downstream sails are more immersed in the upstream wake and the distance between sails is relatively small, indicating a possibly stronger interaction. Comparatively, AWA of 90° means sailing at beam reach condition where ships achieve the highest driving force. At this condition, sails are located at the same streamwise location with the maximum chord-to-chord distance as shown in Fig. 6 (b). These two AWAs are considered representative of great interest, which is why they are chosen here. To better demonstrate the interaction effects, the single sail (SS, only one sail fixed at the position of WS2) simulations are conducted as reference cases for comparison. Mesh topology, boundary conditions, and

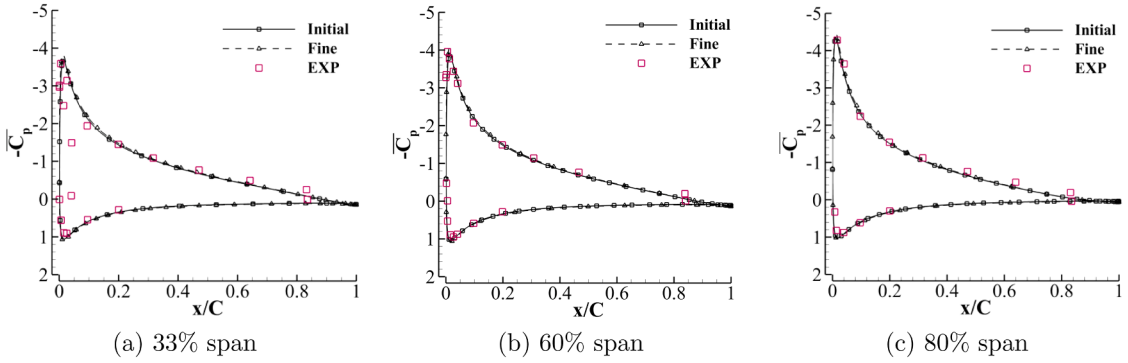

Fig. 5. Comparison of the $\overline{C_p}$ distributions between numerical and experimental data (by Giovannetti et al., 2022).

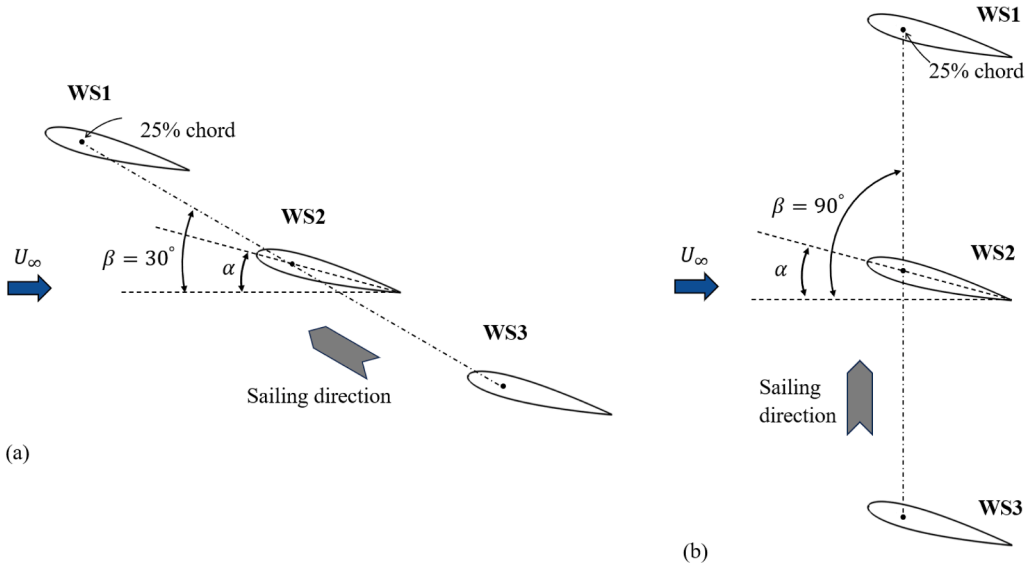

Fig. 6. Schematics of (a) AWA 30° and (b) AWA 90°.

computational domain are kept similar to those of multi-wingsail as discussed in Section 3. More details are provided in the Appendix.

4.1. Angle of attack $\alpha = 10°$

Two multi-wingsail (MW) cases, MW1030 and MW1090 are studied in this section whose AoA α is fixed at 10° with different AWA of 30° and 90°, respectively. Table 3 shows the aerodynamic performance of the two multi-wingsail cases and the single sail (SS10) case at the same AoA. The value of $\langle x \rangle$ calculated by Eq. (4) is the root-mean-square deviation (RMSD) to quantify the level of unsteadiness. Experimental data is also included in Table 3.

$$\langle x \rangle = \sqrt{\frac{\sum_{i=1}^{n} \left(x_i - \overline{x}\right)^2}{n}} \tag{4}$$

where $\overline{x}$ is the time-averaged value and n is the number of samples during the time-span.

The CFD result agrees reasonably well with the experiments, especially in $\overline{C_L}$. $\overline{C_D}$ has comparatively more discrepancy, which can be attributed to the absence of boundary layer tripper in CFD. Since the absolute discrepancy is small and the trend is well captured, the simulation is valid for these two cases.

As shown in Table 3, the MW1030 case achieves the highest $\overline{C_L}$ in its first sail, which even outperforms the single wingsail (SS10) case by 25.8 %. The $\overline{C_L}$ of its second wingsail becomes 16.7 % lower than the SS10 case and the third sail is further reduced. Comparatively, the MW1090 case has a quite different performance. All three wingsails underperform the SS10 case with the mid-sail having the lowest $\overline{C_L}$. For the fluctuating quantities, $\langle C_L \rangle$ and $\langle C_D \rangle$ for both cases are at a much lower magnitude. This indicates the flow is well attached with limited unsteady behaviors. In what follows, the mechanism behind different $\overline{C_L}$ performance trends is discussed together with flow-field details and $\overline{C_p}$ distributions.

Table 3
Aerodynamic performance of wingsails at AoA of 10°.

Cases	MW1030			MW1090			SS10
	WS1	WS2	WS3	WS1	WS2	WS3	WS
$\overline{C_L}$	0.968	0.663	0.489	0.741	0.644	0.668	0.769
$\overline{C_D}$	0.066	0.060	0.038	0.047	0.045	0.043	0.042
$\langle C_L \rangle$	$1.3e^{-3}$	$0.95e^{-3}$	$0.62e^{-3}$	$3.9e^{-3}$	$1.8e^{-3}$	$2.3e^{-3}$	$2.5e^{-3}$
$\langle C_D \rangle$	$2.5e^{-4}$	$2.0e^{-4}$	$1.2e^{-4}$	$6.9e^{-4}$	$3.2e^{-4}$	$4.9e^{-4}$	$5.4e^{-4}$
$\overline{C_L}$ EXP	0.920	0.636	0.452	0.693	0.671	0.684	-
$\overline{C_D}$ EXP	0.030	0.085	0.054	0.052	0.051	0.046	-

Fig. 7 plots the $\overline{C_p}$ distributions at 50 % span of the three wingsails of MW1030 and single sail SS10. WS1, located in the most upstream has a higher suction peak than WS2. Similarly, WS2 has a higher suction peak than its downstream WS3. This is because the upstream sails generate a downwash effect for the downstream sails that moves their stagnation

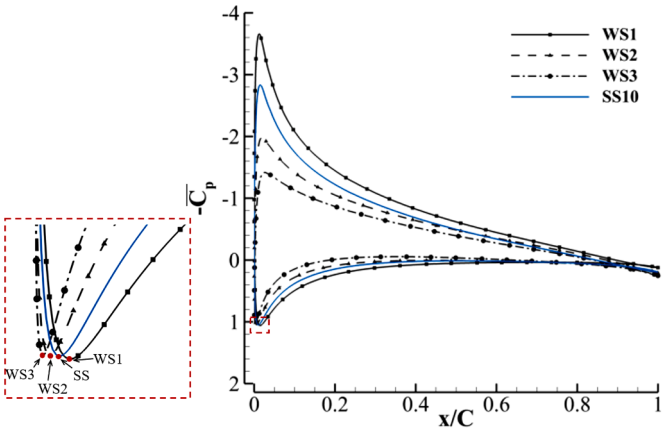

Fig. 7. $\overline{C_p}$ distributions at 50 % span of MW1030 and SS10.

points upstream for a reduced circulation. This can be observed in the zoom-in view in Fig. 7 where the stagnation point of WS3 is located the most upstream due to the downwash effect. Note that the downwash effect discussed here does not refer to the one generated by the tip vortex. To better demonstrate this downwash effect, Fig. 8 (a) shows the time-averaged y-directional velocity ($\overline{v}$) contours with 2D streamlines. $\overline{v}$ becomes significantly lower immediately upstream the WS2 and WS3 with streamlines more deflected towards negative y-direction. To quantify this downwash effect, flow quantities are extracted from the dashed-dot lines at $0.6C$ upstream of each sail. Fig. 8 (b) plots the change of angle of attack ($\Delta\alpha$) due to the downwash effect using $\Delta\alpha = \arctan(\overline{v}/\overline{u})$. Usually, when the free-stream reaches an airfoil, it bifurcates at the stagnation point near the leading edge (LE) with a portion of it flowing around the LE, generating an upwash velocity (positive v). This is what is experienced by WS1 which leads to a positive $\Delta\alpha$ about 4.2° ~ 5.4°. However, due to the downwash effect, $\Delta\alpha$ becomes about 0° for WS2 and around -2° for WS3, lower than that of the SS10 case. It is noteworthy that the levels of reduction in $\Delta\alpha$ among WS1, WS2, and WS3 correspond to the levels of reduction in suction peaks as observed in Fig. 7. Overall, the downwash effect induced by the upstream sails reduces the downstream flow angles and moves the stagnation points toward the upstream. Therefore, the wingsails' loading is decreased for a worse aerodynamic performance.

So far, we have explained how the performance of downstream sails is deteriorated, however, the remaining question of interest is how the upstream WS1 is positively affected by the downstream sails since it possesses a higher suction peak than the SS10 case. As shown in Fig. 8 (a), the downstream WS2 generates an upwash effect near its LE. As this upwash effect propagates upstream, it suppresses the negative $\overline{v}$ field at the pressure side of WS1 with less deflected streamlines as compared to the SS10 case in the top-right of Fig. 8 (a). As a result, streamlines stagnate on a more downstream location, leading to the enhancement of the suction peak. Similarly, WS2 is also subjected to the upwash effect from WS3, which partially offsets the downwash effect from WS1 and, therefore ends up with a medium performance between WS1 and WS3.

As the AWA increases to 90°, the three sails are located in the same streamwise location, suggesting that the interaction from downstream or upstream is minimized. However, performance variation still exists as indicated in Table 3 where WS1 and WS3 have higher $\overline{C_L}$ than WS2. To understand this, Fig. 9 (a) shows the $\overline{C_p}$ contours of the MW1090 and SS10 cases and their $\overline{C_p}$ distributions at 50 % span are shown in Fig. 9 (b). Predominantly, the performance variation is due to the pressure-field interactions between adjacent wingsails. For WS1, its pressure surface is adjacent to the suction surface of WS2. The high-pressure field (HPF) at the pressure side and low-pressure field (LPF) at the suction side affect each other in a negative way that leads to a reduced performance for both sails. Similarly, the pressure fields of WS2 and WS3 interact in the same way. Since both sides of WS2 are negatively affected, it ends up with the worst performance among the three sails. The suction side of WS1 and pressure side of WS3 have no adjacent sails, and are, therefore less affected. The $\overline{C_p}$ distribution in Fig. 9 (b) shows that the pressure side of WS3 virtually overlaps with that of SS10 and that the suction side of WS1 also locates closely with SS10 with a slight enhancement due to the increase of local wind speed. However, the other side of WS1 and WS3 that is adjacent to WS2 is negatively affected, which makes their overall performance worse than SS10.

4.2. Angle of attack α = 17°

Table 4 compares the aerodynamic performance of MW1730, MW1790, and SS17. Similarly, the root mean square deviation and experimental data are also presented. At low AWA, MW1730 has the highest $\overline{C_L}$ in WS1, and descends in the following wingsails, similar to its performance at α = 10°. However, the differences lie in the fluctuating quantities where α = 17° case has significantly higher $\langle C_L \rangle$

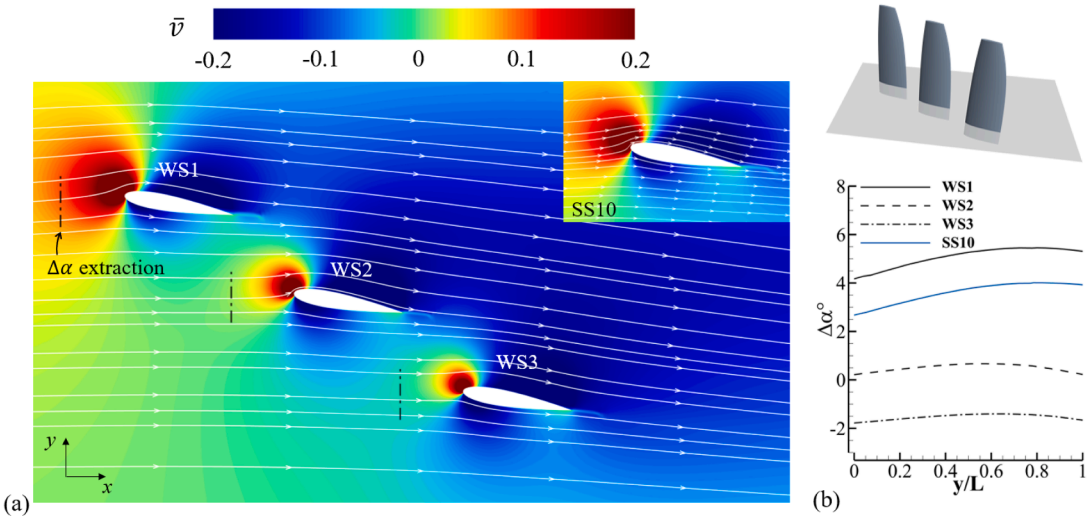

Fig. 8. Flow field results of MW1030: (a) time-averaged $\overline{v}$ contours and streamlines of MW1030 at 50 % span, SS10 case in the top-right figure; (b) Distributions AoA variation ($\Delta\alpha$) extracted along the dashed-dot line in figure (a).

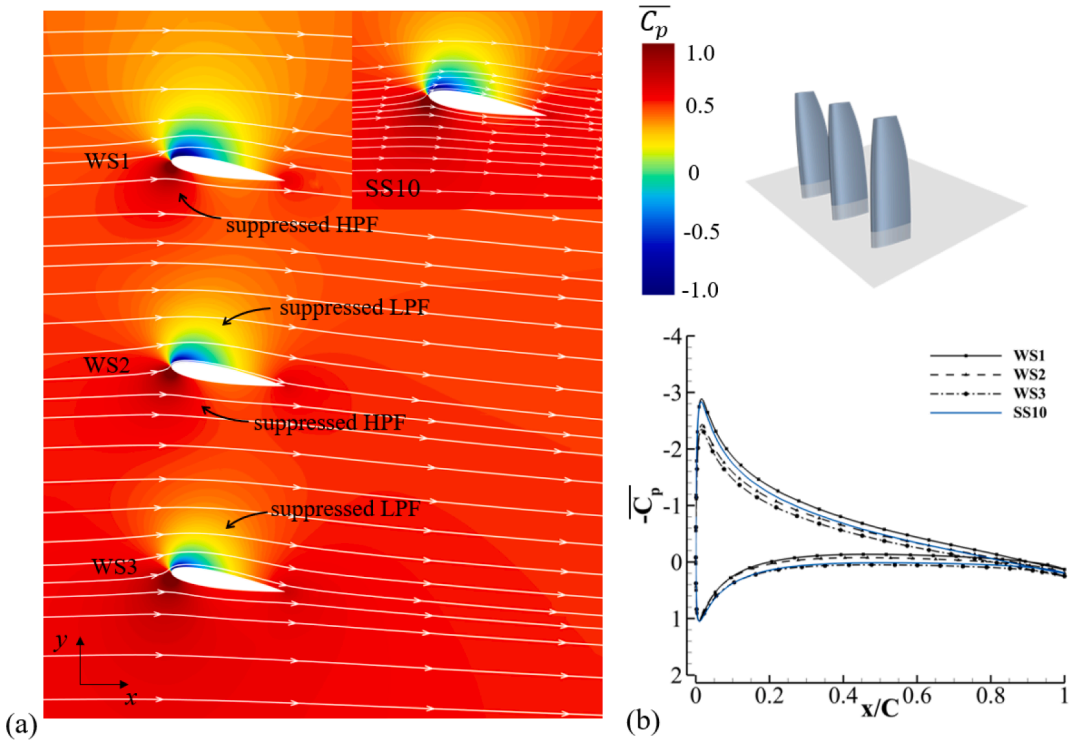

Fig. 9. Flow field results of MW1090: (a) time-averaged $\overline{C_p}$ contours and streamlines of MW1090 and SS10 at 50 % span; (b) $\overline{C_p}$ distributions at 50 % span of MW1090 and SS10.

Table 4
Aerodynamic performance of wingsails at AoA of 17°.

Cases	MW1730			MW1790			SS17
	WS1	WS2	WS3	WS1	WS2	WS3	WS
$\overline{C_L}$	1.376	1.156	0.819	1.222	1.058	1.006	1.078
$\overline{C_D}$	0.143	0.139	0.144	0.097	0.096	0.087	0.122
$\langle C_L \rangle$	$2.4e^{-2}$	$1.1e^{-2}$	$6e^{-3}$	$2e^{-3}$	$1e^{-3}$	$1e^{-3}$	$2.5e^{-2}$
$\langle C_D \rangle$	$6.0e^{-3}$	$3.0e^{-3}$	$9e^{-4}$	$4e^{-4}$	$3e^{-4}$	$3e^{-4}$	$6.0e^{-3}$
$\overline{C_L}$ EXP	1.325	1.016	0.830	0.755	0.796	0.862	-
$\overline{C_D}$ EXP	0.126	0.199	0.135	0.242	0.228	0.196	-

and $\langle C_D \rangle$, over 20 times increase in WS1 as compared to the MW1030 case. The single wingsail SS17 has a similar fluctuating magnitude. The discussion provided in this section aims to understand the physics behind such force fluctuations. For high AWA, the WS2 of MW1790 no longer has the lowest $\overline{C_L}$ but ranks the middle among the three sails. The fluctuating quantities are substantially smaller than the MW1730 case, indicating a better-attached flow. In comparison with experimental data, the MW1730 case achieves a good agreement, whereas the prediction of MW1790 is quite off. More explanation will be provided later.

Fig. 10 plots the $\overline{C_p}$ distributions at two spanwise locations of the MW1730 case and the SS17 case. At the 50 % span shown in Fig 10 (a), the $\overline{C_p}$ distributions are alike those of MW1030 case with the strongest suction peak in WS1, followed by SS17, WS2, and WS3, sequentially. This is caused by the same combinatorial effects of downwash and upwash flows as discussed before. However, at lower 15 % span, WS1 and SS17 have significantly reduced suction peak, and a pressure plateau region ($0.2 < x/C < 1.0$) (Xu et al., 2021; Xu et al.(2022)Xu, Ren and Zha) exists for both sails. No pressure plateau exists for WS2 and WS3. For a better understanding, Fig. 11 shows the time-averaged velocity magnitude ($\overline{V_m}$) contours at 15 % for MW1730 and SS17. The pressure plateau corresponds to the flow separation on WS1 and SS17, which results from the increased AoA with a higher adverse pressure gradient (APG). Although flow separation occurs, WS1 generates sufficient downwash effects that help the flow restore attachment on WS2 and WS3. Under the downstream upwash effect, WS1 is operated at a higher AoA, which makes the flow separation even stronger than that of SS17. Fig. 12 shows the isosurface of the instantaneous Q-criterion at 200,000 with the 3D streamlines extracted from the time-averaged flow field. Flow separation is sourced from the wind tunnel floor. This is because the floor boundary layer retards the low span free-stream, and with the combined effect of the high APG at a high AoA of 17°, flow separation occurs. Since WS2 and WS3 operate under the downwash effect with reduced aerodynamic loading, the low-span free stream, even though retarded by the near-wall boundary layer, can still attach to these wingsails.

Fig. 13 shows the instantaneous pressure coefficient (C_p) contours of the MW1730 and SS17 case at 15 % span. On each wingsail, the low-C_p region near the leading edge (LE) represents the suction side acceleration zone. In WS1, the low-C_p region expands to the entire chord with a shedding pattern, which results from the flow separation. A similar low-C_p region is also observed in the aft-chord of the SS17 case, however, the size is significantly smaller due to the absence of the upwash effect from stream. This also aligns with the observations in Q-criteria and velocity contours as shown in Figs. 11 and 12.

As indicated by Table 4, fluctuating quantities become more significant in the current high AoA. To study the wingsails' interaction effect on fluctuating quantities, we conduct power spectrum density (PSD) analysis on the histories of C_L and C_D for SS17 and MW1730 cases. As shown in Fig. 14 (a), SS17 has a single spike at the Strouhal number ($St_H = fC/U_\infty$) of 0.09, whereas the MW1730 possesses two dominant spikes as shown in Fig. 14 (b) and (c), one at a similar St_H of 0.08 and the other one at a higher St_H of 0.13. This indicates that under the interaction effect, the low-frequency fluctuation becomes more complicated in MW1730. To better understand the responsible motions for these spikes, we conducted proper orthogonal decomposition (POD) for

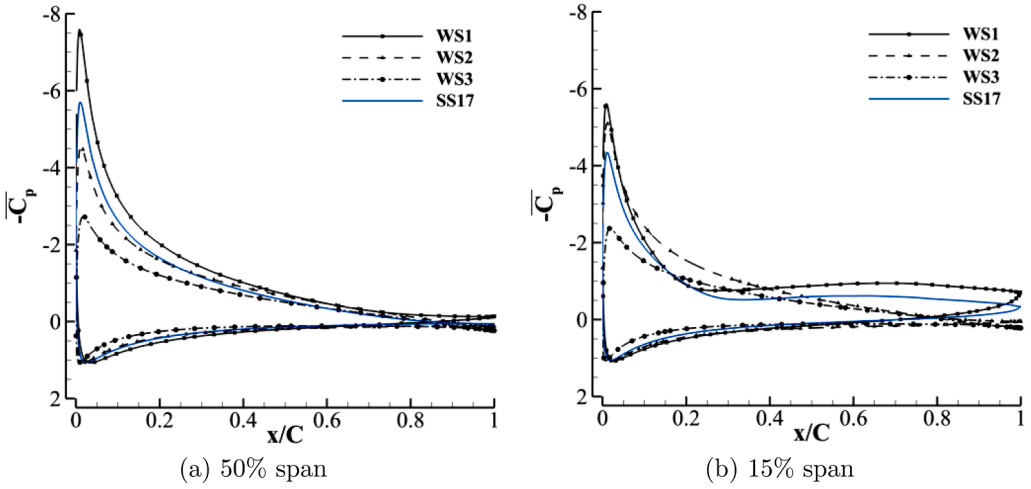

Fig. 10. $\overline{C_p}$ distributions of MW1730 and SS17 at span 50 % and 15 %.

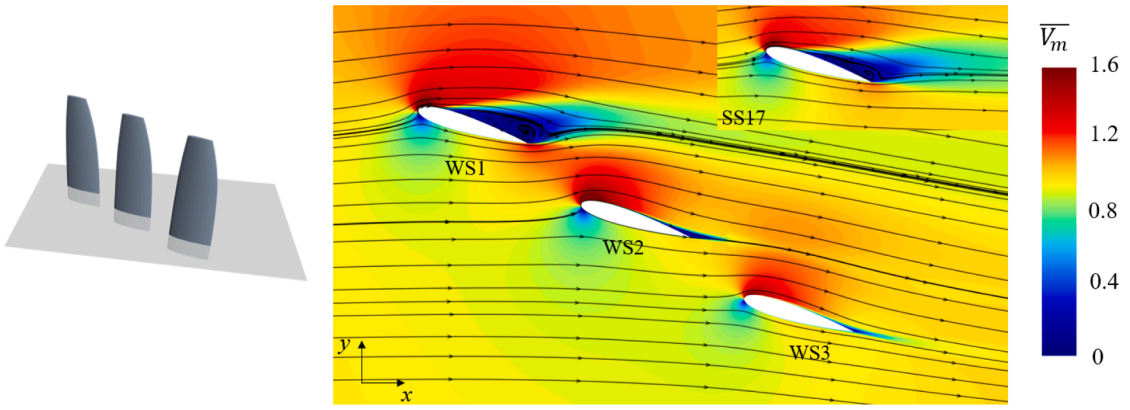

Fig. 11. Time-averaged velocity magnitude ($\overline{V_m}$) contours at 15 % span of MW1730 and SS17 cases.

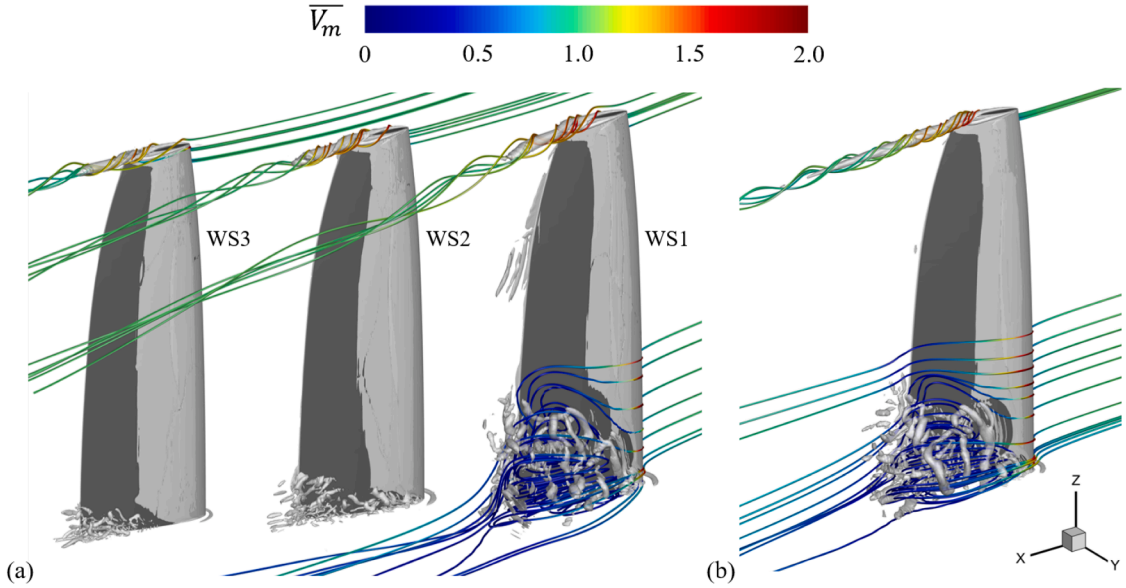

Fig. 12. 3D streamlines colored by $\overline{V_m}$ and instantaneous Q-criteria at 200000: (a) MW1730 and (b) SS17.

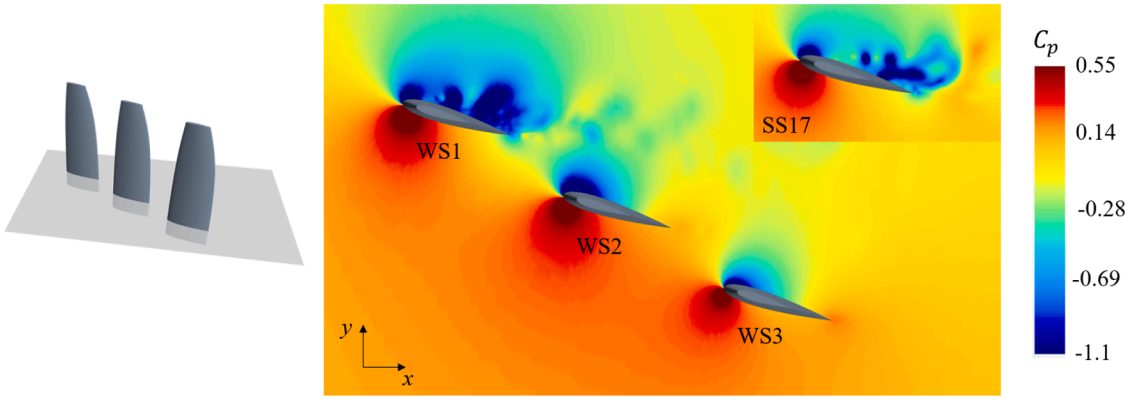

Fig. 13. The instantaneous pressure contours at 15 % span of MW1730 and SS17 cases.

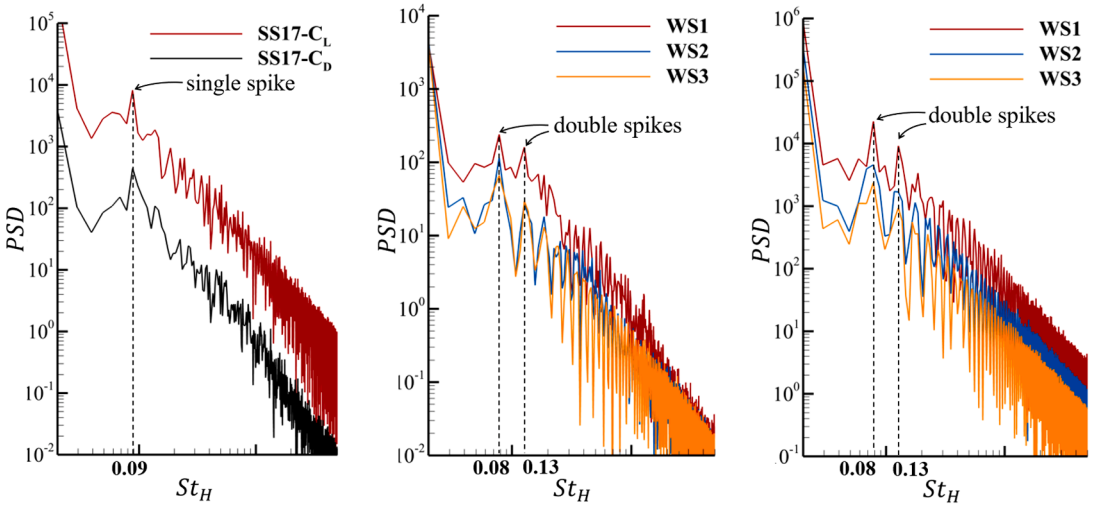

Fig. 14. Power spectrum density of lift and drag coefficients.

both cases at 15 % span location where the flow separation and vortex shedding are severe as shown in Fig. 12.

The data sampling time is approximately $t^* = 180$ with a sampling frequency of 500 Hz. The data processing routine follows the practice in Ref. Östh et al. (2014); Xu et al. (2023, 2024). The sampling frequency of 500 Hz corresponds to ten times the time-step (2×10^{-4}) used in the simulation, which leads to the highest reliable frequency (Nyquist frequency) of 250 Hz, $St_H = 4$. Figs. 15 (a) and 16 (a) show the energy fraction of the first ten modes of the two cases. Since the first three modes account for more than 15 % ~ 20 % of total energy, their corresponding motions are considered representative and are adopted for detailed analysis. The SS17 case's spatial distributions (φ) of Modes 1–3 are shown in Fig. 15 with time-averaged 2D streamlines. The corresponding PSD analysis of the temporal coefficient is also presented in the right column. Mode 1 has a spike at $St_H = 0.09$, the same as those of C_L and C_D in Fig. 14. Mode 1 is, therefore, responsible for the force fluctuations in the SS17 case. In the spatial distribution, Mode 1 has two anti-correlated regions starting from the mid-chord to the trailing edge (TE) on the suction side. This is connected with the periodic vortical behavior in chord-wise direction. In Modes 2 and 3, the low-frequency spike no longer exists and is replaced by two high-frequency spikes. Multiple anti-correlated regions are observed downstream of the wingsail as shown in Fig. 15 (b) and (c). These regions appear alternatively, suggesting a propagation of disturbance, which is a typical pattern of vortex shedding. The orbit plot based on Modes 2 and 3 is shown in Fig. 15 (e) with a clear circular shape, indicating that both modes capture a coherent shedding behavior (Berkooz et al., 1993). This can also be supported by the energy fraction plot in Fig. 15 (a), where Modes 2 and 3 have a similar energy level as a modal pair. However, these sheddings at high frequency correspond to the small-scale fluctuations, which is why they are not prominent on the force PSD plots in Fig. 14 (a). For the MW1730 case shown in Fig. 16, Mode 1 has two dominant frequencies, aligning with the two spikes respectively in Fig. 14 (b) and (c). Different from the SS17 case, Mode 2 is also dominated by a low-frequency spike at $St_H = 0.13$. Since the spatial distributions of both Mode 1 and Mode 2 present a chord-wise anti-correlated region, this means the low-frequency vortical behavior is enhanced in MW1730 case. Such an enhancement can be attributed to the interaction effect. Under the interaction effect, WS1 has an increased aerodynamic loading with a higher AoA than the SS17 case. The separated shear layer at the LE feeds the separation bubble with more circulation and makes the vortical motion more vigorous (Gerrard, 1966; Green and Gerrard, 1993). Mode 3 has a high-frequency spike occurs. Its spatial distribution has anti-correlated region elongated more downstream following a streamwise direction instead of chord-wise, reflecting the vortex shedding. A dynamically-coupled behavior is indicated by the circular orbit plot based on Modes 3 and 4 in Fig. 16 (e), which is also supported by the similar energy levels of both modes. Due to the enhanced

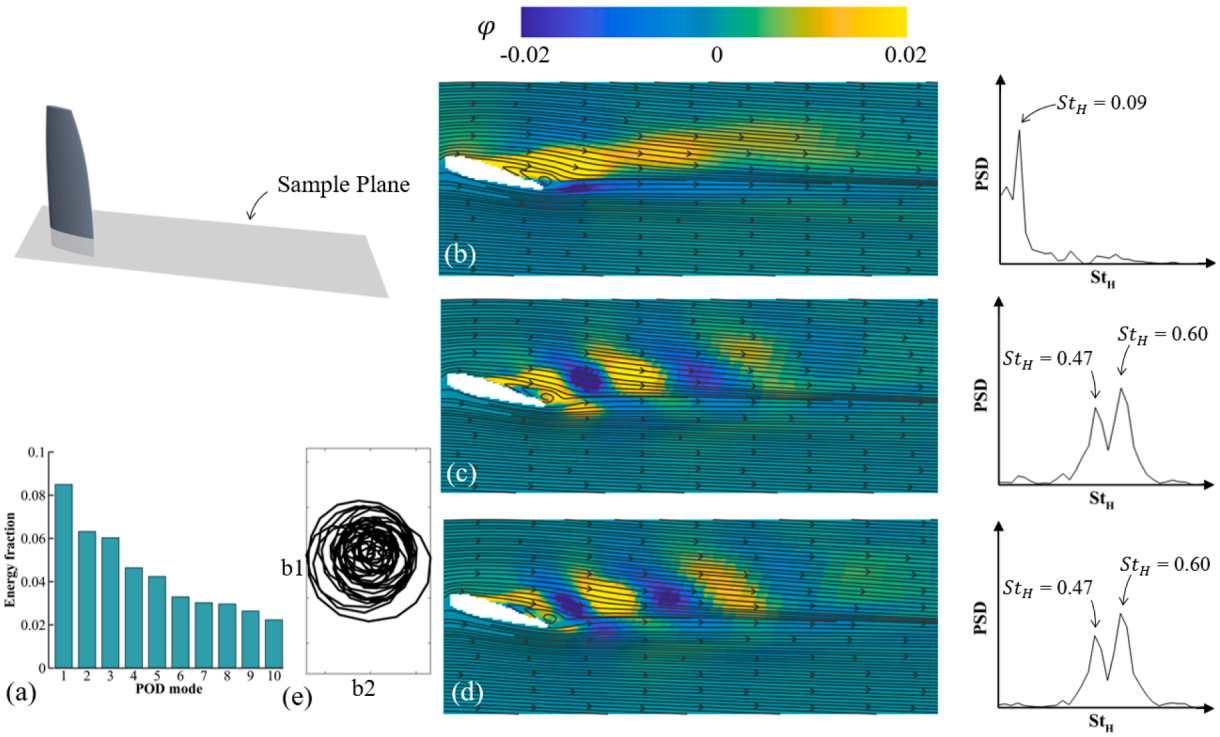

Fig. 15. Proper orthogonal decomposition (POD) analysis of SS17 at 15 % span: (a) energy fraction of the first-ten POD modes; the spatial distributions and temporal coefficient of (b) Mode 1, (c) Mode 2, and (d) Mode 3; (e) orbit plot of shedding modes.

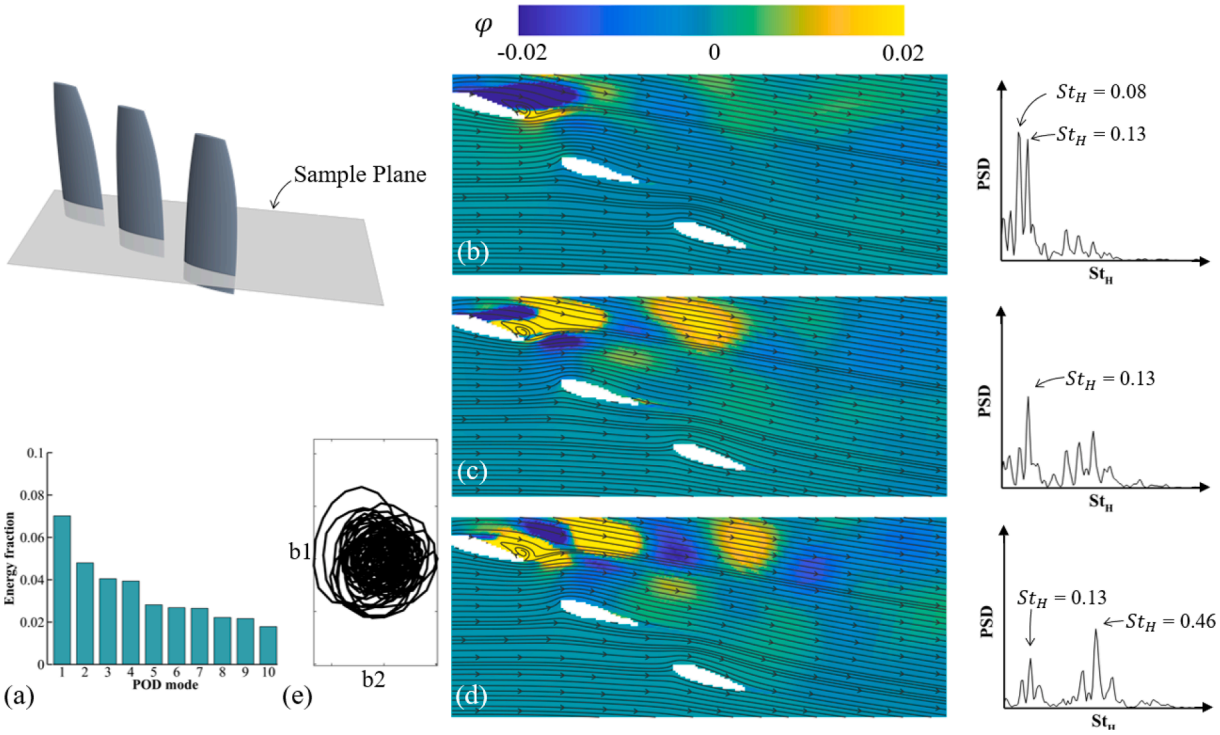

Fig. 16. Proper orthogonal decomposition (POD) analysis of MW1730 at 15 % span: (a) energy fraction of the first-ten POD modes; the spatial distributions and temporal coefficient of (b) Mode 1, (c) Mode 2, and (d) Mode 3; (e) orbit plot of shedding modes.

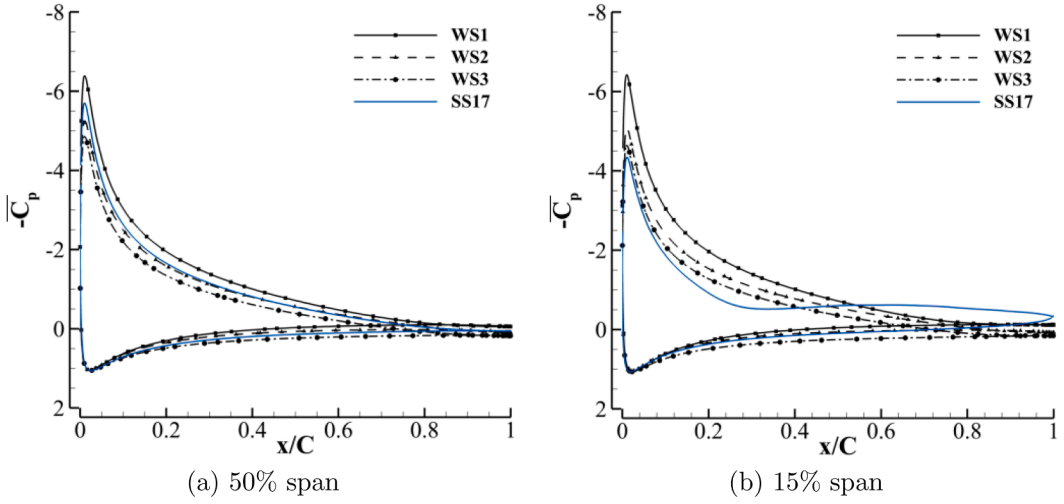

Fig. 17. $\overline{C_p}$ distributions of MW1790 and SS17 at span 50 % and 15 %.

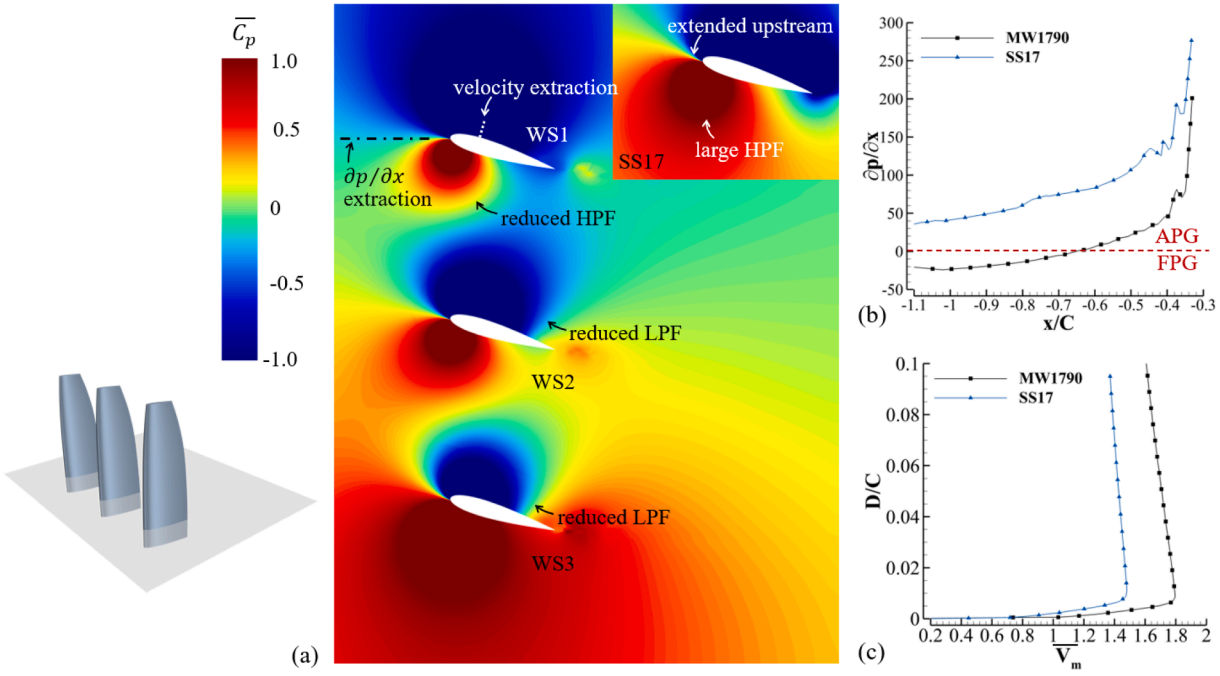

Fig. 18. Flow-field results at 15 % of MW1790 and SS17 case: (a) $\overline{C_p}$ contours, (b) Pressure gradients ($\partial p/\partial x$) ahead of WS1, (c) Velocity profiles of WS1 and SS17 at 23 %C downstream the leading edge.

vortical motion in MW1730 case, the anti-correlated region in Mode 3 not only manifests in the x-direction but also the y-direction as shown in Fig. 16 (b)-(d). This means the shedding disturbance also propagates downwards to WS2 and WS3, which is why these two wingsails possess similar force fluctuating patterns even though the flow is well-attached.

Overall, the PSD and POD analysis demonstrated that the force fluctuation in the SS17 case is attributed to a chord-wise vortical motion. With the effects of the downstream wingsails in MW1730, WS1 has significantly higher circulation with a severer flow separation. The vortical behavior becomes more vigorous, leading to an enhanced force fluctuation.

Fig. 17 plots the $\overline{C_p}$ distributions of the MW1790 and SS17 cases at 50 % and 15 % spans. Fig. 18 shows the $\overline{C_p}$ contours at 15 % span. For both spans in Fig. 17, the surface $\overline{C_p}$ of both sides of the wingsails increases from WS1 to WS3 as the $\overline{C_p}$ plots are shifted downwards. This is because, from WS1 to WS3 the high-pressure field on the pressure side becomes less affected by the low-pressure field from the adjacent sail, which increases the overall field pressure near WS3, as shown in Fig. 18 (a). As presented in Table 4, WS2 no longer has the lowest $\overline{C_L}$ as it is at 10° AoA due to the enhanced suction peak at higher AoA. As the overall field pressure increases from WS1 to WS3, the penalty of suction peak outweighs the improvement of pressure-side pressure, which leads to the lowest $\overline{C_L}$ in WS3.

At 15 % span, the pressure plateau observed in SS17 case no longer exists in MW1790, meaning that the suction-side flow separation does not occur in the multiple wingsail cases. Among the three sails, the suction side of WS2 and WS3 can benefit from the downwash flow induced by their adjacent sails, which is less likely to stall. Therefore, our interest is confined to investigating why WS1 does not stall. The reason again can

be attributed to the interactions between low- and high-pressure fields. As shown in Fig. 18 (a), the high-pressure field (HPF) of WS1 is constrained by the suction side low-pressure field (LPF) from WS2, leading to a contracted area as compared to the single sail case. The suction-side low pressure of WS1 can, therefore, extend more upstream, which affects the upstream pressure gradient. Fig. 18 (b) plots the streamwise pressure gradient ($\partial p/\partial x$) from $1.1C$ to $0.3C$ ahead of the leading edge of the SS17 and WS1. Extraction locations are indicated in Fig. 18 (a). As flow approaches the wingsail, WS1's $\partial p/\partial x$ has a favorable pressure gradient (FPG) followed by a mild adverse pressure gradient, whereas the SS17 has the entire upstream region covered by APG and the $\partial p/\partial x$ is remarkably higher than that of the WS1. Flow experiencing the high APG becomes more sluggish when it reaches the sail surface. Fig. 18 (c) compares the velocity profiles between SS17 and MW1790 at the location of 23 %C downstream of the leading edge on the suction surface. The velocity profile of SS17 is 16.7 % weaker than that of the WS1, which is prone to the flow separation (Xu et al.(2022)Xu, Ren and Zha; Xu et al., 2021, 2020). This explains why the flow separation occurs at the SS17 case but not at MW1790.

Nevertheless, Table 4 suggests that the predicted $\overline{C_L}$ of MW1790 is much higher than the experiments and that $\overline{C_D}$ is significantly smaller. This suggests that the experiments stall earlier than the CFD prediction. Aside from the boundary layer tripper effects that are not considered in simulations, this mismatch can result from a particular experimental operation during testing. As reported in Ref. Malmek (2023), in order to rotate wingsails at a high AoA of approximately 17° ∼ 19°, the experiment has to reduce the wind speed to 10 m/s for rotation operation, and then increase to the test speed of 25 m/s due to the mechanical load limits. It was found that lowering and ramping up the speed generated a hysteresis effect, where the wingsails stalled at lower angles of attack. Since the current study focuses on the interaction effects among wingsails, the effort to understand this mismatch is considered out of scope and will be continued in a future study.

5. Conclusions

A model-scale three-wingsail system is numerically studied to understand the interaction mechanism behind the performance variations of multiple wingsails. The numerical simulations are conducted using Improved Delayed Detached Eddy Simulation (IDDES) with $k-\omega$ SST model in Star-CCM+. The numerical setups are validated by experimental data by Giovannetti et al. (2022). The current study investigates two angles of attack (AoAs), a lower one of 10° and a higher one of 17°. At each AoA, two apparent wind angles (AWAs) of 30° and 90° are studied, standing for representative interactive scenarios.

Results show that flow is well attached at low AoA. The interaction at AWA of 30° results from the downwash and upwash effects generated by the upstream and downstream wingsails, respectively. The downwash effect moves the pressure-side stagnation point upstream with reduced AoA and circulation, leading to a deteriorated performance in downstream sails. Comparatively, the upstream wingsail benefits from the upwash effect generated from the leading edge (LE) of downstream wingsails, which ends up with enhanced performance, even outperforming the single sail case. At AWA of 90° where the wingsails are located in the same streamwise position, the interaction effect is caused by pressure-field interaction between the adjacent pressure side and the suction side from adjacent wingsails. This generally impairs the performance in both ways.

As AoA increases to 17°, flow separations occur at the low-span of the WS1 and the single sail due to the sluggish flow in the floor boundary layer. The flow separation is more severe in WS1 than in the single sail case because the downstream upwash effect further increases the first sail's AoA. Associated with the flow separation, force fluctuations become more significant as measured by the root mean square deviations of lift coefficient ($\langle C_L \rangle$) and drag coefficient ($\langle C_D \rangle$). The analysis based on power spectrum density (PSD) and proper orthogonal decomposition (POD) suggests that the interaction effect promotes the vortical motion at the high AoA and makes the force fluctuation stronger.

CRediT authorship contribution statement

Kewei Xu: Writing – review & editing, Writing – original draft, Visualization, Validation, Software, Methodology, Investigation, Funding acquisition, Formal analysis, Data curation, Conceptualization; **Karolina Malmek:** Writing – review & editing, Validation, Formal analysis, Data curation; **Rickard Bensow:** Writing – review & editing, Validation, Supervision, Resources, Project administration, Investigation, Funding acquisition, Data curation, Conceptualization.

Declaration of competing interest

The authors declare that they have no known competing financial interests or personal relationships that could have appeared to influence the work reported in this paper.

Acknowledgment

This work is supported by Chalmers University of Technology, Area of Advance Transport. The computations were enabled by resources provided by the National Academic Infrastructure for Supercomputing in Sweden (NAISS) at Tetralith partially funded by the Swedish Research Council through grant agreement no. 2022–06725. The authors would like to thank Prof. Sinisa Krajnovic for the support in computational resource. The authors would like to acknowledge the project: Energimyndigheten under the project numbers P51553-1 and P2021-00275. The authors also extend their gratitude to the WPCC/Oceanbird research group (Dr. L. Marimon Giovannetti, U. Dhomé, K. Malmek, A. Persson, and C. Wielgosz) at RISE Research Institutes of Sweden and KTH Royal Institute of Technology for providing wind tunnel test results and their valuable inputs. The lead author would also like to acknowledge the start-up funding provided by the Office of the Vice President for Research and Dean of the Graduate School, University of Maine.

Appendix: Numerical setups of single sail cases

This appendix is to provide additional details regarding the numerical setups of the single sail cases, SS10 and SS17, which are used in the main text to demonstrate the multi-wingsails' interaction effects. Similar to the MW cases, SS cases adopt the exact wind tunnel geometry as the computational domain, and the sail is placed at the position of the mid-sail (WS2). Fig. 19 shows the mesh details of SS17 case. A similar mesh topology with the combination of O- and H-type grids is adopted here. The overall mesh size contains 25 million cells for the initial mesh. The first grid distance of wingsail surfaces Δy is 1.2×10^{-5}m to ensure $y^+ = \frac{\Delta y u_\tau}{\nu}$ lower than 1. There are 40 cells placed within 10 %C near the wingsail surface for boundary layer refinement. The y^+ of wind tunnel walls is 49. The chord-wise and spanwise resolutions are kept the same with MW cases. The mesh dependency study is conducted using a fine mesh of 35 million cells. The refinement is mainly in the wingsail normal direction and streamwise direction in the downstream to better resolve the wake. Table 5 shows $\overline{C_D}$ and $\overline{C_L}$ acquired from initial and

Table 5
Mesh dependency study of SS10 and SS17 cases.

Cases	SS10		SS17	
	$\overline{C_L}$	$\overline{C_D}$	$\overline{C_L}$	$\overline{C_D}$
Initial	0.769	0.0420	1.078	0.122
Fine	0.765	0.0418	1.070	0.121
Δ	0.52 %	0.47 %	0.74 %	0.82 %

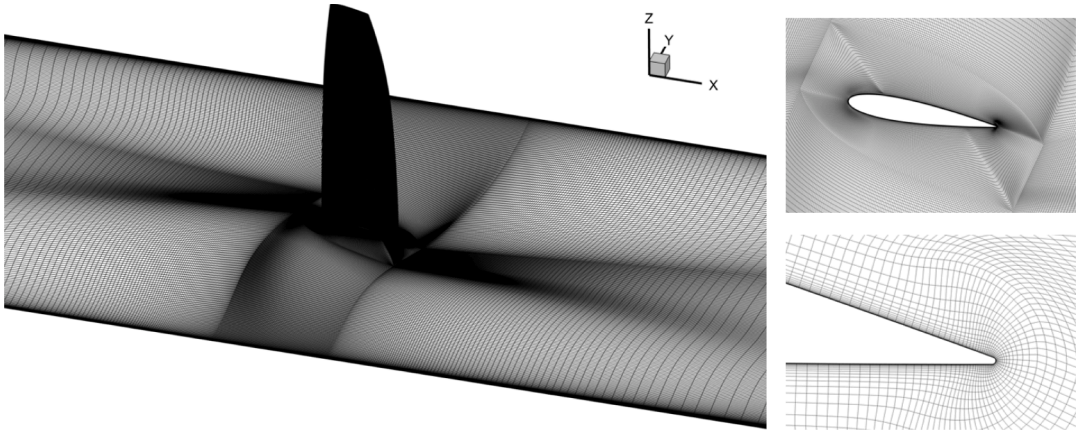

Fig. 19. Mesh topology for single sail cases.

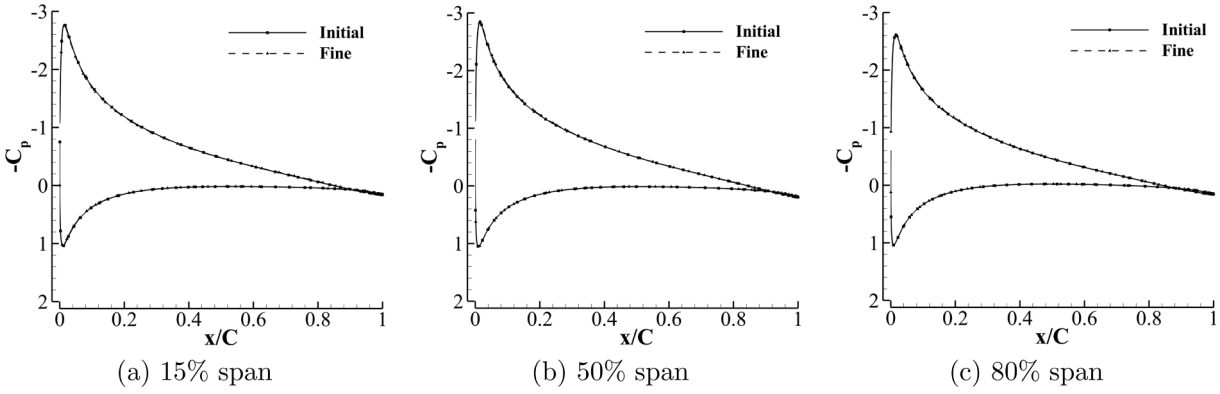

Fig. 20. $\overline{C_p}$ distributions for initial and fine mesh of SS10.

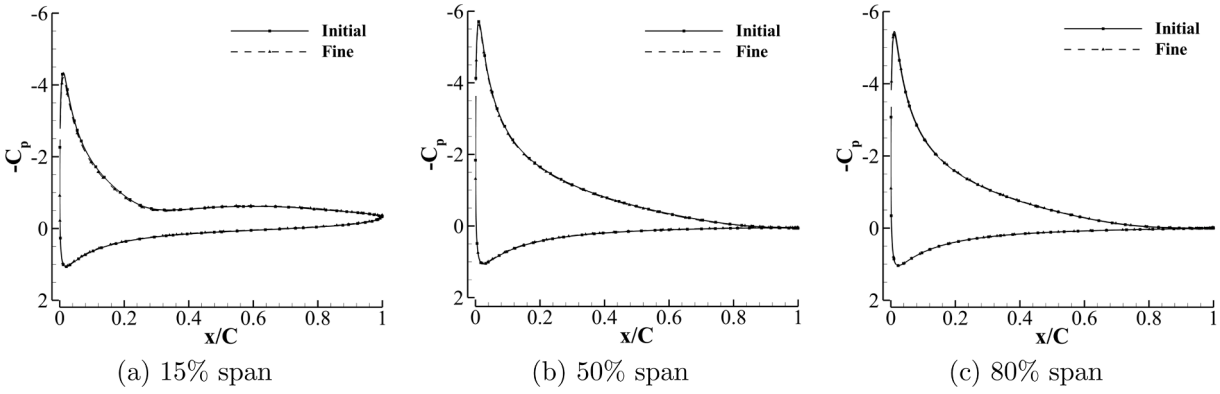

Fig. 21. $\overline{C_p}$ distributions for initial and fine mesh of SS17.

fine meshes. SS17 case has a slightly higher discrepancy due to the flow separation at the low span. Nevertheless, the overall dependency (Δ) is less than 1 %. Figs. 20 and 21 plot the $\overline{C_p}$ distributions at the spans of 15 %, 50 %, and 80 %, which virtually overlap with one another. Overall, the mesh refinement study indicates that the initial mesh is capable of predicting the single sail at AoA of 10° and 17°, and the solution is converged based on the mesh size of 25 million cells.

References

Atkinson, G.M., 2019. Analysis of lift, drag and CX polar graph for a 3D segment rigid sail using CFD analysis. J. Marine Eng. Technol. 18 (1), 36–45. https://doi.org/10.1080/20464177.2018.1494953

Berkooz, G., Holmes, P., Lumley, J.L., 1993. The proper orthogonal decomposition in the analysis of turbulent flows. Annu. Rev. Fluid Mech. 25 (1), 539–575.

Bordogna, G., January 2020. Aerodynamics of wind-assisted ships: Interaction effects on the aerodynamic performance of multiple wind-propulsion systems. Ph.D. Dissertation, Delft University of Technology, Delft, Netherlands https://doi.org/10.4233/uuid:96eda9cd-3163-4c6b-9b9f-e9fa329df071

Cairns, J., Vezza, M., Green, R., MacVicar, D., 2021. Numerical optimisation of a ship wind-assisted propulsion system using blowing and suction over a range of wind conditions. Ocean Eng. 240, 109903. https://doi.org/10.1016/j.oceaneng.2021.109903

Fujiwara, T., Hearn, G.E., Kitamura, F., Ueno, M., 2005. Sail–sail and sail–hull interaction effects of hybrid-sail assisted bulk carrier. J. Mar. Sci. Technol. 10, 82–95. https://doi.org/10.1007/s00773-005-0191-4

Gentry, A., 1981. A review of modern sail theory. In: Proc. 11th AIAA Symposium on the Aero/Hydronautics of Sailing, Seattle, Washington, USA.

Gentry, A., 1971. The aerodynamics of sail interaction. In: Proceedings of the Third AIAA Symposium on the Aero/Hydronautics of Sailing, Redondo Beach, California, USA.

Gerrard, J.H., 1966. The mechanics of the formation region of vortices behind bluff bodies. J. Fluid Mech. 25 (2), 401–413. https://doi.org/10.1017/S0022112066001721
Giovannetti, L.M., Dhome, U., Malmek, K., Persson, A., Wielgosz, C., 2022. Multi-wing sails interaction effects. In: SNAME Chesapeake Sailing Yacht Symposium, Maryland, USA. SNAME. https://doi.org/10.5957/CSYS-2022-006
Green, R.B., Gerrard, J.H., 1993. Vorticity measurements in the near wake of a circular cylinder at low reynolds numbers. J. Fluid Mech. 246, 675–691. https://doi.org/10.1017/S002211209300031X
IMO, 2023. 2023 IMO Strategy on reduction of GHG emissions from ships 15, 1–17.
Khan, L., Macklin, J., Peck, B., Morton, O., Souppez, J.-B. R.G., 15 Sept., 2021. A review of wind-assisted ship propulsion for sustainable commercial shipping: latest developments and future stakes. In: Wind Propulsion Conference, London, UK. Royal Institution of Naval Architects. https://doi.org/10.3940/rina.win.2021.05
Kleinert, J., Ehrle, M., Waldmann, A., Lutz, T., 2024. Wake tail plane interactions for a tandem wing configuration in high-speed stall conditions. CEAS Aeronaut. J. 15 (1), 79–103.
Lee, H., Jo, Y., Lee, D.-J., Choi, S., 2016. Surrogate model based design optimization of multiple wing sails considering flow interaction effect. Ocean Eng. 121, 422–436. https://doi.org/10.1016/j.oceaneng.2016.05.051
Lehmann, F.-O., Sane, S.P., Dickinson, M., 2005. The aerodynamic effects of wing–wing interaction in flapping insect wings. J. Exp. Biol. 208 (16), 3075–3092. https://doi.org/10.1242/jeb.01744
Li, Q., Nihei, Y., Nakashima, T., Ikeda, Y., 2015. A study on the performance of cascade hard sails and sail-equipped vessels. Ocean Eng. 98, 23–31. https://doi.org/10.1016/j.oceaneng.2015.02.005
Malmek, K., 2023. Rapid Aerodynamic mMethod for iInteracting Sails. Chalmers Tekniska Hogskola (Sweden).
Malmek, K., Larsson, L., Werner, S., Ringsberg, J.W., Bensow, R., Finnsgård, C., 2024. Rapid aerodynamic method for predicting the performance of interacting wing sails. Ocean Eng. 293, 116596. https://doi.org/10.1016/j.oceaneng.2023.116596
Myose, R.Y., Hayashibara, S., Yeong, P.-C., Miller, L.S., 1997. Effect of canards on delta wing vortex breakdown during dynamic pitching. J. Aircr. 34 (2), 168–173. https://doi.org/10.2514/2.2168
Oceanbird, 2021, https://www.theoceanbird.com/. Concept design of a car carrier.
Östh, J., Noack, B.R., Krajnović, S., Barros, D., Borée, J., 2014. On the need for a nonlinear subscale turbulence term in POD models as exemplified for a high-reynolds-number flow over an ahmed body. J. Fluid Mech. 747, 518–544. https://doi.org/10.1017/jfm.2014.168
Ouchi, K., Uzawa, K., Kanai, A., June, 2011. Huge hard wing sails for the propulsor of next generation sailing vessel. In: The Second International Symposium on Marine Propulsors, Hamburg, Germany.
Persson, A., Li, D.-Q., Olsson, F., Werner, S., Dhome, U., 2019. Performance prediction of wind propulsion systems using 3D CFD and route simulation. In: 6th International Conference on Computational Methods in Marine Engineering, Rome, Italy June 2015. Royal Institution of Naval Architects, pp. 19–30. https://doi.org/10.3940/rina.win.2019.03
Shah, S., Ahmed, A., 2024. On the secondary stall of a wing in tandem configuration. Aeronaut. J. , 1–14.
Smith, T. W.P., Jalkanen, J.P., Anderson, B.A., Corbett, J.J., Faber, J., Hanayama, S., Okeeffe, E., Parker, S., Johansson, L., Aldous, L., et al., 2015. Third IMO greenhouse gas study 2014.
Tay, W.B., 2017. Effect of different types of wing-wing interactions in flapping MAVs. J. Bionic Eng. 14 (1), 60–74. https://doi.org/10.1016/S1672-6529(16)60378-5
Tu, E.L., 1994. Vortex-wing interaction of a close-coupled canard configuration. J. Aircr. 31 (2), 314–321. https://doi.org/10.2514/3.46489
Viola, I.M., Biancolini, M.E., Sacher, M., Ubaldo, C., 2015. A CFD-based wing sail optimisation method coupled to a VPP. In: 5th High Performance Yacht Design Conference, Auckland, New Zealand.
Wielgosz, C., Dhomé, U., Blackert, E., Giovannetti, L.M., Wallin, S., Kuttenkeule, J., Werner, S., 2025. The importance of scale effects for wind propulsion: experimental and numerical analysis of a wing sail. In: SNAME Chesapeake Sailing Yacht Symposium, Maryland, USA. SNAME.
Xu, K., Su, X., Bensow, R., Krajnovic, S., 2023. Large eddy simulation of ship airflow control with steady coanda effect. Phys. Fluids 35 (1). https://doi.org/10.1063/5.0127560
Xu, K., Su, X., Jonsson, I., Bensow, R., Krajnovic, S., 2024. Numerical study of a generic ship's airwake for understanding bi-stability mechanism. J. Fluid Mech. 991, A6. https://doi.org/10.1017/jfm.2024.511
Xu, K., Ren, Y., Zha, G., 2022. Numerical analysis of energy expenditure for coflow wall jet separation control. AIAA J. 60 (5), 3267–3285. https://doi.org/10.2514/1.J061015
Xu, K., Ren, Y., Zha, G., 2020. Numerical investigation of NASA hump using co-flow jet for separation control. In: AIAA Scitech 2020 Forum, Orlando Florida, USA, AIAA 2020-1058, p. 1058. https://doi.org/10.2514/6.2020-1058
Xu, K., Ren, Y., Zha, G.-C., 2021. Separation control by co-flow wall jet. AIAA AVIATION 2021 FORUM, VIRTUAL EVENT, AIAA Paper 2020–2954. https://doi.org/10.2514/6.2021-2946
Xu, K., Zha, G.-C., 2021. High control authority three-dimensional aircraft control surfaces using coflow jet. J. Aircr. 58 (1), 72–84. https://doi.org/10.2514/1.C035727
Zhu, H., Yao, H.-D., Ringsberg, J.W., 2024. Unsteady RANS and IDDES studies on a telescopic crescent-shaped wingsail. Ships Offshore Struct. 19 (1), 134–147. https://doi.org/10.1080/17445302.2023.2256601
Zhu, H., Yao, H.-D., Thies, F., Ringsberg, J.W., Ramne, B., 2023. Propulsive performance of a rigid wingsail with crescent-shaped profiles. Ocean Eng. 285, 115349. https://doi.org/10.1016/j.oceaneng.2023.115349